PIER C

Current Sensor Fault Detection and Fault-Tolerant Control of Bearingless Induction Motor Based on VCS

Shihan Zhan[1], Zebin Yang[1,*], Xiaodong Sun[2], and Qifeng Ding[1]

[1] *School of Electrical and Information Engineering, Jiangsu University, Zhenjiang 212013, China*
[2] *Automotive Engineering Research Institute, Jiangsu University, Zhenjiang 212013, China*

ABSTRACT: To ensure the normal operation of a control system for a bearingless induction motor (BIM) after current sensor failure, a virtual current sensor (VCS) fault-tolerant control strategy was proposed. First, on the basis of the coordinate transformation of the stator current of the torque winding, the fault detection marks were set to realize current sensor fault detection. Second, according to the mathematical models of BIM, the stator current differential equations included in the VCS were derived, and the solutions of the equations were used as the reconstruction current of the fault current sensor, achieving fault-tolerant operation control after the sensor fault. The simulated and experimental results show that the set fault detection marks can realize the quick and accurate identification of sensor faults, and the estimated current from the VCS output can replace the faulty current after the current sensor fails, and the stator current can be reconstructed effectively under no-load, load change, and speed change conditions, and also ensure a good suspension of the motor rotor under sudden addition of disturbance condition.

1. INTRODUCTION

Bearingless motor (BM) is a new type of motor that realizes the functions of rotor suspension and rotation. It uses the structural similarity between its stator and the magnetic bearing, stacking the winding that produces the magnetic bearing suspension force into the stator slots. To provide a steady suspension and rotation of the rotor, two sets of windings that produce the radial force work together to suspend the rotor [1]. The BMs not only possess all the benefits of magnetic bearings, but also have the benefits of small, high-power density, and being simple to increase in speed and power. Therefore, BMs have numerous potential applications in particular industrial fields including high-speed centrifuges, flywheel energy storage, and artificial heart pumps [2–4]. Among them, the bearingless induction motor (BIM) is characterized by its uniform air gap, low cost, high mechanical strength, and considerable radial suspension force produced by the same controlled current, and is one of the most widely studied bearingless motors.

The drive system unavoidably malfunctions because of the heavy load, increased demand for motor speed, and constant changes in the environment. It has the following three main fault types: motor failure [5, 6], inverter failure [7, 8], and sensor failure [9, 10]. The system will fluctuate and perhaps crash because of these issues; thus, the technology for fault diagnosis (FD) and fault-tolerant control (FTC) provides a useful method for early failure detection and for ensuring safe and dependable operation of the motor [11, 12].

Several sensors have been employed as part of the BIM control system to collect voltage, current, and speed signals [13, 14]. On the one hand, the motor can still run normally

without the voltage feedback signal, but it cannot work normally without a current feedback signal [15–17]. However, the complexity of the working environment and the impact of human error will cause problems and even damage to the existing sensor, and the current loop in the BIM control system becomes uncontrollable once the current sensor fails, which causes the current, speed, and other data to change dramatically. At the same time, owing to the coupling between the two BIM windings, the dramatically changing torque winding current also has an impact on the suspension winding current. Finally, this impact causes the suspension of BIM to become unstable. Thus, it is essential to focus on fault detection and FTC of BIM current sensors.

To correctly follow and estimate the three-phase current for power switch faults and current sensor faults, an internal sliding mode observer (SMO) for three-level neutral point clamped (NPC) inverters was developed in [18], and a method for identifying the two fault types was proposed utilizing the sum of anticipated current and measured current. However, the different on-off states of the NPC increase the amount of computation required for the SMO. According to the fractional-order model reference adaptive control for achieving FTC, a back-propagation neural network was proposed in [19] to identify the different forms of sensor faults. However, the performance of neural networks is affected by the fault sample size, which affects fault judgment accuracy. Reference [20] proposes a strategy for IGBT's open circuit fault diagnosis and early fault diagnosis of current sensor in PMSM inverters. This strategy uses incremental and non-singular transformations to decouple the inverter system, which can effectively distinguish the two fault types and constructs a synovium observer to evaluate the reconfiguration state of the subsystem. But it was only for PMSM in-

---

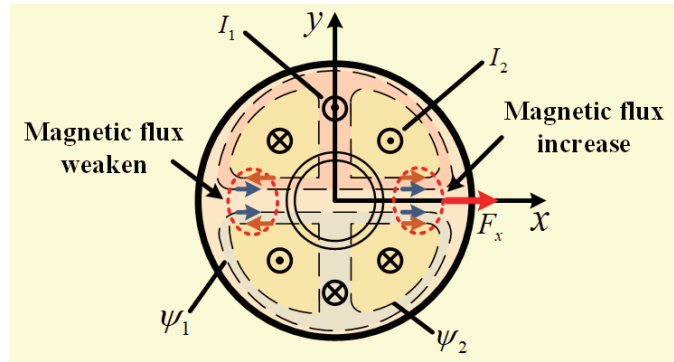* Corresponding author: Zebin Yang (zbyang@ujs.edu.cn).

FIGURE 1. Diagram of generating controlled suspension forces.

verters, and no other motor systems are considered. For sensor faults detection and FTC, different methods, such as observers based [21], date-driven [22], and model-based [23], have also been utilized. There were also problems, such as complex design and calculation, which lengthened the time required to locate faults and decreased the system's operational reliability.

To deal with the current sensor fault in the BIM control system, this paper proposes a fault detection mark and introduces an FTC approach based on the BIM parameter deducing the VCS. First, the coordinate transformation of the three-phase torque winding current in the BIM was completed, and then, the fault detection marks were established using the current from the transformation described above. A faulty sensor can be identified quickly and precisely according to the relationship between the mark differences. Second, VCS was determined based on the inverter DC voltage, motor speed, and partial parameters of the BIM mathematical model. This strategy can better achieve the current estimation of the torque winding after failure and overcome the coupling of the torque winding and suspension winding, which maintains a good BIM suspension while ensuring basic current feedback, and is an effective method in the field of BIM sensor control. Through experimentation and BIM simulations, the usefulness of the proposed strategy was confirmed.

2. BIM SUSPENSION PRINCIPLE AND MATHEMATI-CAL MODEL

2.1. The Suspension Principle of the BIM

The BIM realized rotation and suspension through the joint action of the torque and suspension windings. To produce a controllable radial suspension force, the two sets of windings need to satisfy $p_1 = p_2 \pm 1$ and $p_1 = p_2$, and they produce magnetic fields that rotate in the same direction, where p_1 and p_2 are the electric angular frequencies of the torque and suspension windings, respectively, and p_1 and p_2 are the pole numbers of the corresponding windings.

The BIM torque generation was the same as that of the induction motor, which was created by the Lorentz force, in which the rotor's cutting of the magnetic field is produced, and the Maxwell force, which causes suspension of the BIM. This study takes BIM with $p_1 = 1$ and $p_2 = 2$ as an example, and the sus-

pension principle is shown in Fig. 1. The torque and suspension windings pass the stator currents I_1 and I_2, respectively, and stator fluxes ψ_1 and ψ_2 are superimposed on the x positive axis and weakened at the x negative axis. Consequently, the positive x-axis is where the combined Maxwell force is produced. Similarly, if a suspension force of x negative axis is required, the direction of the two sets of winding currents can be changed, by changing the phase of the winding current, and the suspension force in the y direction can be controlled.

2.2. The Mathematical Model of the BIM

In the static two-phase orthogonal coordinate system (α-β system), the mathematical model of the BIM torque part is as follows [24, 25]:

voltage equation.

$$
\begin{cases}
U_{s1\alpha} = R_{s1} \cdot i_{s1\alpha} + \dfrac{d\psi_{s1\alpha}}{dt} \\[2mm]
U_{s1\beta} = R_{s1} \cdot i_{s1\beta} + \dfrac{d\psi_{s1\beta}}{dt} \\[2mm]
U_{r1\alpha} = R_{r1} \cdot i_{r1\alpha} + \dfrac{d\psi_{r1\alpha}}{dt} + \omega_m \cdot \psi_{r1\beta} \\[2mm]
U_{r1\beta} = R_{r1} \cdot i_{r1\beta} + \dfrac{d\psi_{r1\beta}}{dt} - \omega_m \cdot \psi_{r1\alpha}
\end{cases}
\tag{1}
$$

flux equation.

$$
\begin{cases}
\psi_{s1\alpha} = L_{s1} \cdot i_{s1\alpha} + L_{m1} \cdot i_{r1\alpha} \\
\psi_{s1\beta} = L_{s1} \cdot i_{s1\beta} + L_{m1} \cdot i_{r1\beta} \\
\psi_{r1\alpha} = L_{m1} \cdot i_{s1\alpha} + L_{r1} \cdot i_{r1\alpha} \\
\psi_{r1\beta} = L_{m1} \cdot i_{s1\beta} + L_{r1} \cdot i_{r1\beta}
\end{cases}
\tag{2}
$$

where 1 represents the torque winding related quantity; s and r represent the stator and rotor winding related quantities, respectively; α and β represent the coordinate axis components in the α-β coordinate system, respectively; and L_{m1} represents the torque winding mutual inductance. The controllable radial suspension force equation of BIM in a rotating two-phase co-

TABLE 1. Relationship between marks difference and fault current sensor.

ΔM_i	F_1	F_2	F_3	Faulty sensor
$\Delta M_1 = \Delta M_2 = \Delta M_3$	0	0	0	None
$\Delta M_1 < \Delta M_3 < \Delta M_2$	1	0	0	Phase A
$\Delta M_2 < \Delta M_1 < \Delta M_3$	0	1	0	Phase B
$\Delta M_3 < \Delta M_1 < \Delta M_2$	0	0	1	Phase C

ordinate system is as follows [26]:

$$\begin{cases} F_x = K \left(i_{s2d} \cdot \psi_{1d} + i_{s2q} \cdot \psi_{1q} \right) \\ F_y = K \left(i_{s2q} \cdot \psi_{1d} + i_{s2d} \cdot \psi_{1q} \right) \end{cases} \quad (3)$$

where $K = \pi \mu \mathrm{p}_1 \mathrm{p}_2 \mathrm{L}_{\mathrm{m2}}/(18_0 \mathrm{rLW}_1 \mathrm{W}_2)$, $\mu_0 = 4\pi \times 10^{-7}$ H/m is the permeability of vacuum, and l and r represent the effective BIM core length and rotor radius, respectively. Effective torque winding and suspension winding turns are represented by W_1 and W_2, respectively. The corresponding quantities for the suspension and torque windings are represented by numbers 1 and 2, respectively.

3. CURRENT SENSOR FAULT DETECTION METHOD

3.1. Mathematical Transformation of Three-Phase Current of Torque Winding

In this study, three current sensors were used to provide the feedback current for the control system. When all current sensors are in normal operation, based on the three-phase symmetry of the BIM stator torque winding, the three-phase stator current vector sum is zero at this time:

$$i_{1A} + i_{1B} + i_{1C} = 0 \quad (4)$$

According to Equation (4), when the three-phase stator current vector sum is not zero, a current sensor failure is detected. However, this formula alone is unable to identify the exact position of the sensor malfunction. First, the positive direction of the α axis of the static two-phase coordinate system is aligned with three-phase stator winding A, and the coordinate transformation of the three-phase current is as follows [27]:

$$\begin{cases} i_{s1\alpha} = \dfrac{2}{3} \left(i_{1A} - \dfrac{1}{2} i_{1B} - \dfrac{1}{2} i_{1C} \right) \\ i_{s1\beta} = \dfrac{\sqrt{3}}{3} \left(i_{1B} - i_{1C} \right) \end{cases} \quad (5)$$

Next, Equation (5) is rewritten using only the two-phase currents of A and B:

$$\begin{cases} i'_{s1\alpha} = i_{1A} \\ i'_{s1\beta} = \dfrac{\sqrt{3}}{3} \left(i_{1A} + 2i_{1B} \right) \end{cases} \quad (6)$$

Finally, according to the three-phase symmetry, the A-phase current in (6) was replaced by the B- and C-phase currents, and

then substituted into (6) to obtain:

$$\begin{cases} i''_{s1\alpha} = - \left(i_{1B} + i_{1C} \right) \\ i''_{s1\beta} = -\dfrac{\sqrt{3}}{3} \left(i_{1A} + 2i_{1C} \right) \end{cases} \quad (7)$$

The six α-β axis current components are obtained from Equations (5) to (7), which are related to the three-phase stator current measured by the current sensor.

3.2. Fault Detection Method

The six current components obtained by coordinate transformation were functions of the stator three-phase current, but the faulty sensor location could not be located. Among the current components obtained by Equations (5) to (7), the components that were sensitive to the same two-phase stator current were squared and summed, and the following three fault detection flags were obtained:

$$\begin{cases} M_1 = \left(i''^2_{s1\alpha} + i^2_{s1\beta} \right) \\ M_2 = \left(i'^2_{s1\alpha} + i''^2_{s1\beta} \right) \\ M_3 = \left(i'^2_{s1\alpha} + i'^2_{s1\beta} \right) \end{cases} \quad (8)$$

According to Equations (5) to (7), as can be observed, mark M_1 only correlated with the measured values of the phases B and C current sensors, and marks M_2 and M_3 were only related to the current measurement values of phases A, C and phases A and B, respectively. Marks M_i ($i = 1, 2, 3$) related to the relevant stator current would change when the current value as detected by the current sensor changed, which provided the basis for identifying the fault current sensor.

Different current sensors failed, and the values of M_i were different. To locate the fault more precisely, the actual control system must compare the values of two adjacent sample periods of the detection mark. The precise location of the fault current sensor was identified using the difference value.

$$\Delta M_i = |M_i(K) - M_i(K-1)|, \quad (i = 1, 2, 3) \quad (9)$$

The sample periods K and $(K-1)$ in Equation (9) are represented by K and $K - 1$, respectively. Within two sample periods after the fault, the fault phase location can be determined by analyzing the difference between the marks. The relationship between the specific mark difference and the fault phase position is shown in Table 1.
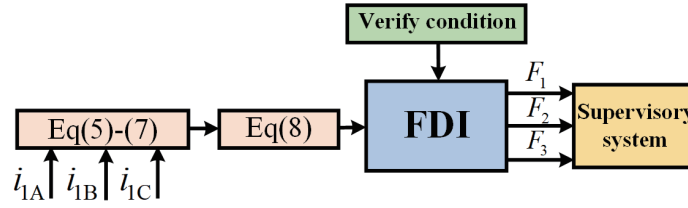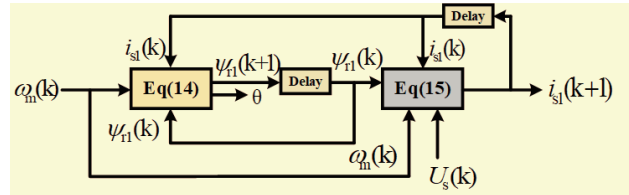
FIGURE 2. Fault isolation flowchart.

FIGURE 3. Virtual current sensor control block diagram.

As illustrated in Table 1, the measured value of the sensor rarely changes in the following two sample periods when there is no current sensor failure: In conjunction with formulas (5) to (7), it is clear that the value of mark M_i ($i = 1, 2, 3$) does not change over the course of the next two sampling periods, and the difference between them calculated by formula (9) is equal to zero. When a sensor fault occurs, the specific fault location can be determined by observing the differences between the marks.

As shown in Fig. 2, (F_1, F_2, F_3) are fault isolation signals, and the signals generated by the faults of the different phase current sensors are different. Following the occurrence of the fault, fault isolation was accomplished by transmitting the isolation signal to the supervision system via the fault detection and isolation unit.

4. FAULT-TOLERANT CONTROL FOR CURRENT SENSOR FAULT

To ensure that the BIM motor operates reliably when the current sensor fails, the system must be subjected to FTC processing after the fault location has been identified. This section proposes the reconstruction of the fault phase current based on the VCS [28, 29] to realize the FTC.

4.1. Derivation of Virtual Current Sensor Algorithm

The mathematical models of BIM are given in the second section, and the rotor current i_{r1} was solved by substituting the rotor winding flux linkage equation into the stator torque winding flux linkage equation to obtain the following equation:

$$\psi_{s1} = \frac{L_{m1}}{L_{r1}} \cdot \psi_{r1} + \left(1 - \frac{L_{m1}^2}{L_{s1} \cdot L_{r1}}\right) \cdot L_{s1} \cdot i_{s1}$$

$$= \frac{L_{m1}}{L_{r1}} \cdot \psi_{r1} + \sigma \cdot L_{s1} \cdot i_{s1} \qquad (10)$$

where $\sigma = 1 - \left(L_{m1}^2 / L_{s1} \cdot L_{r1}\right)$. Simultaneously, Equation (11) was obtained by taking the derivative with time t.

$$\frac{d\psi_{s1}}{dt} = \frac{L_{m1}}{L_{r1}} \cdot \frac{d\psi_{r1}}{dt} + \sigma \cdot L_{s1} \cdot \frac{di_{s1}}{dt} \qquad (11)$$

The differential equations of stator current i_{s1} can be obtained by substituting stator torque winding voltage equation into (11) as follows:

$$\frac{di_{s1}}{dt} = \frac{1}{\sigma \cdot L_{s1}} \left(U_{s1} - R_{s1} \cdot i_{s1} - \frac{L_{m1}}{L_{r1}} \cdot \frac{d\psi_{r1}}{dt}\right) \qquad (12)$$

As the BIM rotor winding coils were closed, the rotor winding voltage was zero. Thus, the rotor current i_{r1} expression was substituted into the rotor winding voltage equation, and the differential equation of rotor flux ψ_{r1} was obtained as follows:

$$\frac{d\psi_{r1}}{dt} = \frac{R_{r1}}{L_{r1}} \cdot (L_{m1} \cdot i_{s1} - \psi_{r1}) - j \cdot \omega_m \cdot \psi_{r1} \qquad (13)$$

The VCS is composed of Equations (12) and (13), which only require the easily obtained parameters of the stator voltage U_{s1} and the motor speed ω_m, and current reconfiguration can be achieved without the need for additional current sensors. Fig. 3 shows the VCS control block diagram.

4.2. Fault-Tolerant Control Strategy

To realize fault tolerant operational control when the current sensor fails, the VCS can estimate the fault phase current. To facilitate the operation of the system microprocessor and prevent the occurrence of algebraic loops in the control system from causing an inability to run, Equations (14) and (15) must be
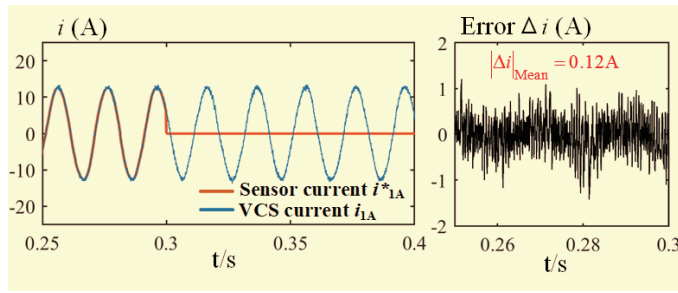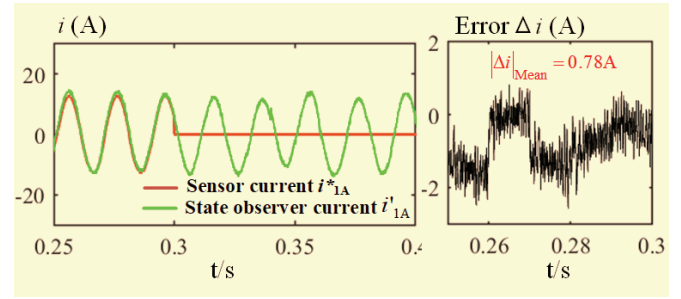
FIGURE 4. Sensor current and VCS current of A-phase.

FIGURE 5. Sensor current and State observer current of A-phase.

TABLE 2. The Parameters of a BIM.

Parameters	Torque Winding	Suspension Winding
Stator resistance (Ω)	2.01	1.03
Rotor resistance (Ω)	11.48	0.075
Mutual inductance of stator and rotor (H)	0.15856	0.00932
Self-inductance of stator (H)	0.00454	0.00267
Self-inductance rotor (H)	0.00922	0.00542
Number of pole pairs	1	2
Rotational inertia (Kg·m^2)	0.00769	0.00769

discretized using the forward Euler method.

$$\begin{cases} \psi_{r\alpha}(k+1) = \psi_{r\alpha}(k) \\ \quad + \left[\dfrac{R_{r1}}{L_{r1}} (L_{m1} \cdot i_{s\alpha}(k) - \omega_m(k) \cdot \psi_{r\beta}(k)) \right] \cdot T_s \\ \psi_{r\beta}(k+1) = \psi_{r\beta}(k) \\ \quad + \left[\dfrac{R_{r1}}{L_{r1}} (L_{m1} \cdot i_{s\beta}(k) - \omega_m(k) \cdot \psi_{r\alpha}(k)) \right] \cdot T_s \end{cases} \tag{14}$$

$$\begin{cases} i_{s\alpha}(k+1) = i_{s\alpha}(k) + \dfrac{1}{L_{s1} \cdot \sigma} \left[U_{s\alpha}(k) - R_{s1} \cdot i_{s\alpha}(k) \right. \\ \quad \left. - \dfrac{L_{m1} \cdot R_{r1}}{L_{r1}^2} (L_{m1} \cdot i_{s\alpha}(k) - \omega_m(k) \cdot \psi_{r\beta}(k)) \right] \cdot T_s \\ i_{s\beta}(k+1) = i_{s\beta}(k) + \dfrac{1}{L_{s1} \cdot \sigma} \left[U_{s\beta}(k) - R_{s1} \cdot i_{s\beta}(k) \right. \\ \quad \left. - \dfrac{L_{m1} \cdot R_{r1}}{L_{r1}^2} (L_{m1} \cdot i_{s\beta}(k) - \omega_m(k) \cdot \psi_{r\alpha}(k)) \right] \cdot T_s \end{cases} \tag{15}$$

In Equations (14) and (15), parameters k and $k+1$ represent the system kth and $(k+1)$th samplings after discretization, and T_s represents the sampling time, which is also the step size in the forward Euler method.

As shown in Fig. 4, the A-phase current sensor failed at 0.3 s. Before the fault occurred, the mean error was 0.12 A. In Fig. 5, the mean error of the fault-tolerant control current obtained by the state observer was 0.78 A. After the fault occurred, the VCS

current value can still maintain stable situation that before sensor fault, but the state observer estimated that the current has a burr and a slight fluctuation. This shows that the VCS current is better than that of the state observer for current reconstruction, and the VCS current can provide feedback in place of the faulty measurement value after sensor failure.

5. ANALYSIS OF SIMULATION RESULTS

MATLAB/Simulink software was used to create a simulation model and conduct simulation research to verify the efficacy of the defect detection approach firstly in this section. The motor parameters utilized in the simulation are listed in Table 2, and the control system is the traditional rotor field-oriented control. The VCS-based system control block diagram is shown in Fig. 6. When a current sensor fault occurs, the control system enters FTC mode, and the feedback current and rotor flux linkage are estimated by the VCS. The parameters $i_{s1\alpha\beta}^{VCS}$ and i_{1ABC} represent the estimated current and the current measurement that the current sensor feeds back into the system, respectively.

5.1. Analysis of Fault Detection Performance

In this section, the simulated verification is performed on B phases. The failure time of the B-phase current sensor was at 0.5 s.

As shown in Fig. 7, within the two sampling periods after the sensor fault occurred, the value of the detection marks was generated owing to the failure. Combined with the data in Table 1, the location of the faulty current sensor could be determined. After the fault occurred, the fault isolation signal was immediately generated and input into the supervision system, and the isolation of the fault phase current sensor was realized. In addi-
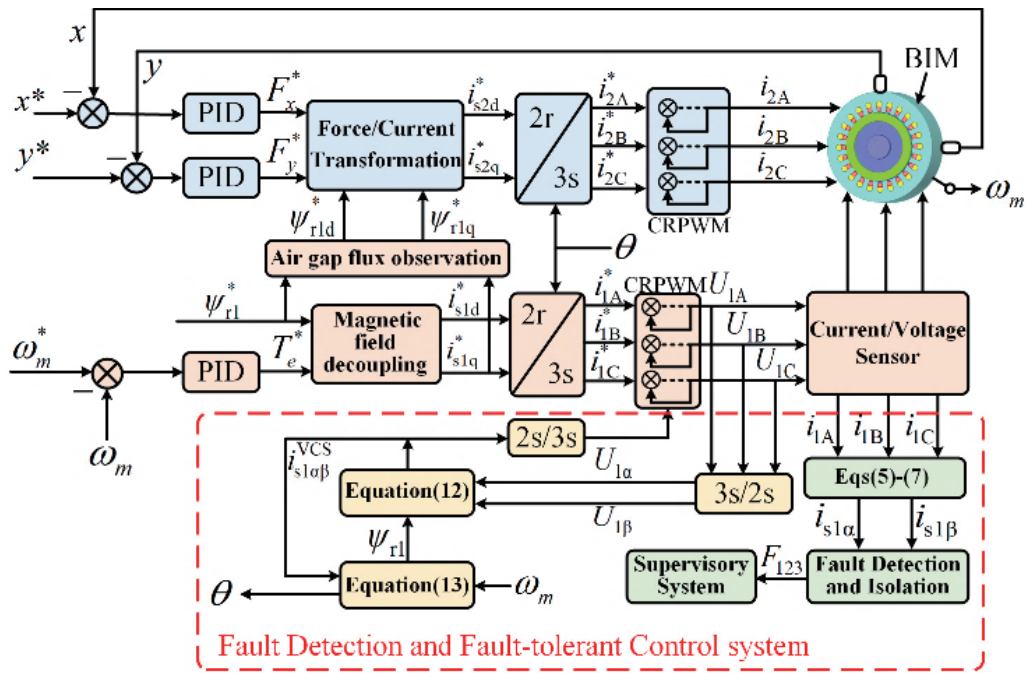
FIGURE 6. Principle control block diagram of fault detection and fault tolerance control for BIM current sensors.
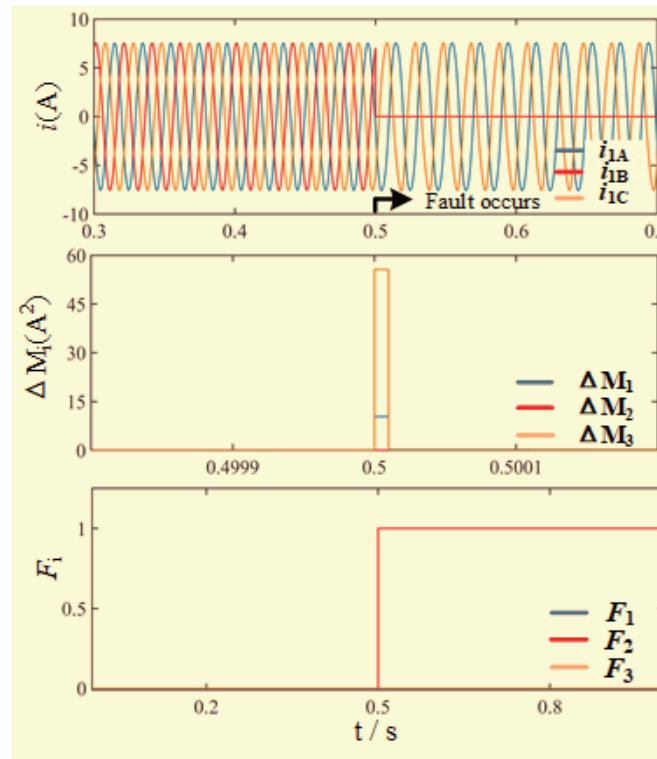

FIGURE 7. Current sensor fault situation of phase B.

tion, the isolated signals caused by other faulty current sensor still satisfy the quantitative relationship shown in Table 1. The fault detection method designed in this study is effective and accurate for a control system containing three current sensors.

Under actual working conditions, BIM runs at different speeds. When the BIM motor was under no load, the current sensor fault detection at low and rated speeds was simulated to verify the feasibility of the fault detection method at various
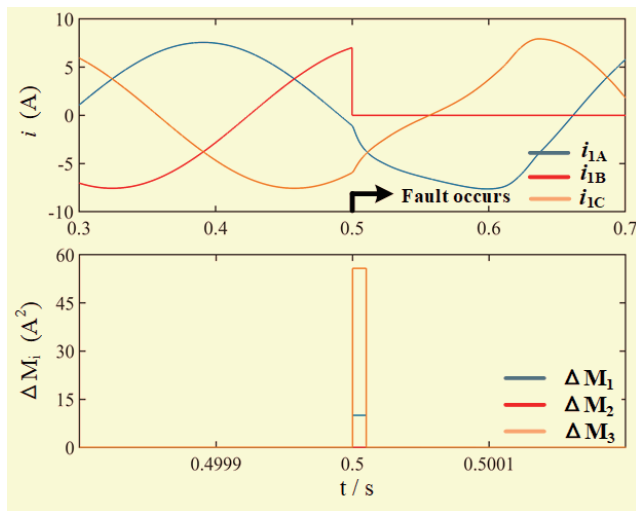
FIGURE 8. Current sensor fault detection at no load and low speed of phase B.
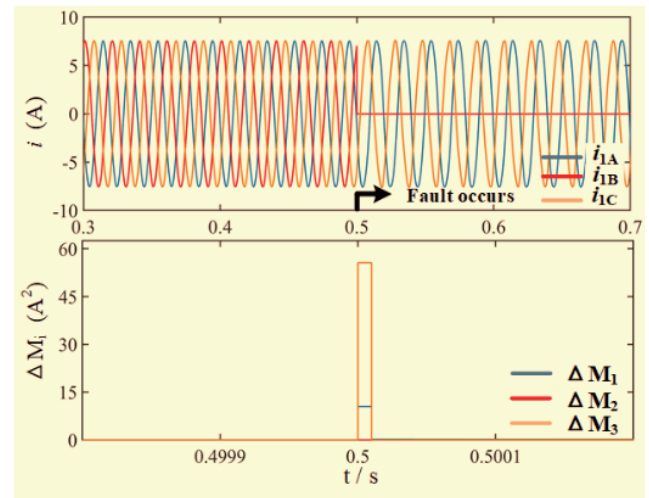
FIGURE 9. Current sensor fault detection at no load and rated speed of phase B.
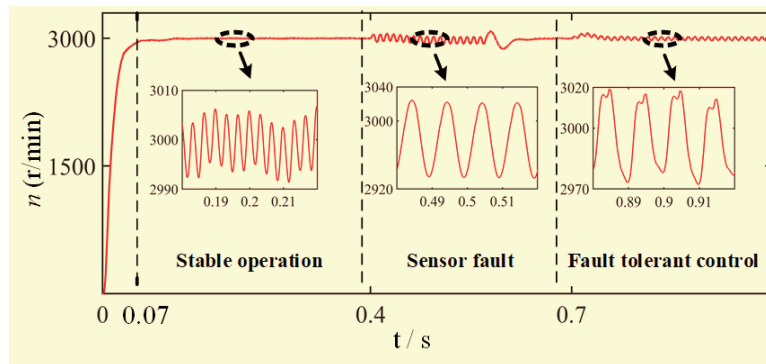
FIGURE 10. Speed of the BIM in different stage.

speeds. The rated speed of the motor was 3000 r/min, and the low speed was 150 r/min.

As shown in Fig. 8, the B-phase current sensor failed at 0.5 s, which caused the faulty phase stator current to reach zero at low speed, causing other two-phase stator currents to be distorted; thus, the value of the detection mark was utilized to identify the faulty phase location. The stator current of the faulty phase has little effect on the other two phases while the motor was operating at its rated speed, as shown in Fig. 9, and the detection mark can also accurately output the fault value, which was used to identify the location of the faulty current sensor. As can be observed, whether the BIM was operating at low speed or rated speed, under no-load conditions, the fault location of the current sensor could be precisely identified with the fault detection approach proposed in this paper.

5.2. Analysis of Fault-Tolerant Control Performance

5.2.1. Performance Analysis at Different Running Stages

Speed is an indicator that must be considered to verify that the motor was running stably. This section simulates the effect of

fault-tolerant operation control on the speed when the current sensor fails.

According to Fig. 10, the BIM's rated speed was $n* = 3000$ r/min. There was a current sensor fails at 0.4 s, and the control system switched to fault-tolerant operation control at 0.7 s. In the stable operation stage, the speed error was within ± 10 r/min. The current feedback of the control system was no longer accurate because of the current sensor failure. The speed fluctuated greatly, and its error reached 80 r/min ~40 r/min. After entering the fault-tolerant operation control, the estimated current of the VCS was used to substitute the measured current of the faulty sensor, and the speed error decreased to -30 r/min ~20 r/min compared with the fault stage. After sensor failure, the actual speed can be better followed by the rated speed, and the motor operating reliability requirements are satisfied. This fault-tolerant method can ensure better speed performance of BIM after current sensor failure.

5.2.2. Analysis of Variable Speed Operation

Figure 11(a) depicts the diagram for speed variations, as well as a comparison of the estimated current of the VCS and the ref-
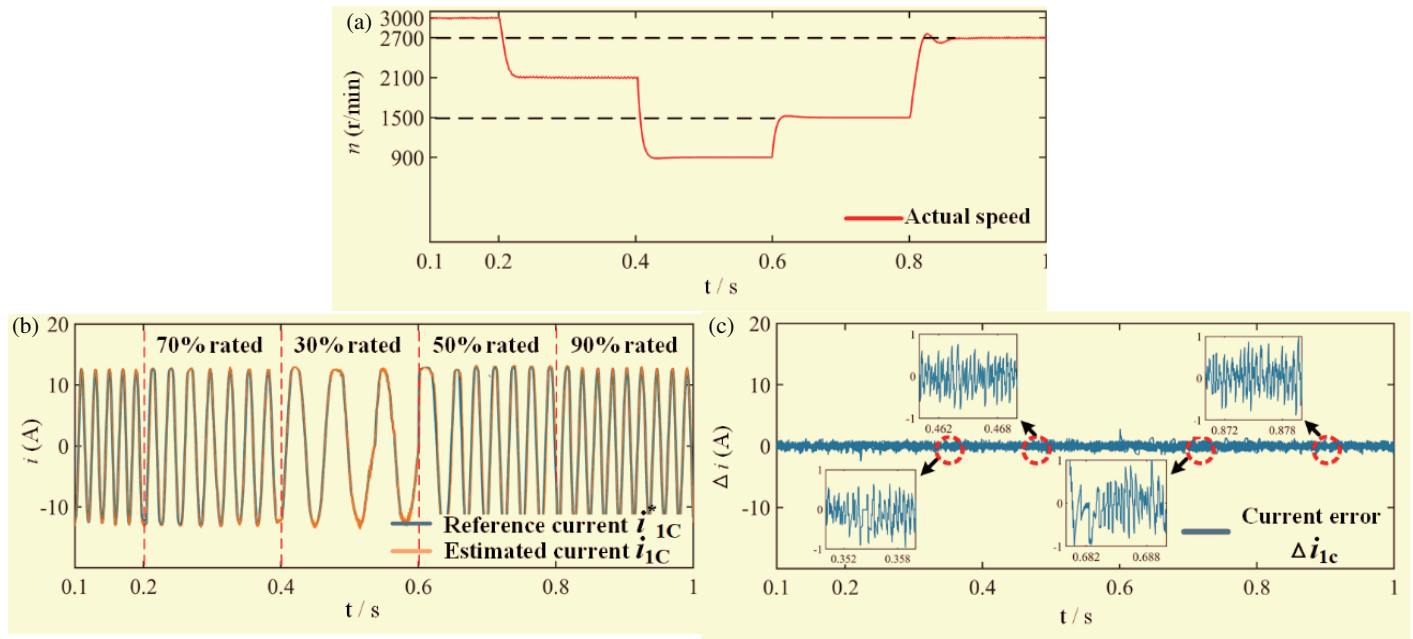
FIGURE 11. FTC current under speed variation. (a) Speed variation under FTC. (b) Reference current and estimated current under speed variation. (c) Current error under speed variation.
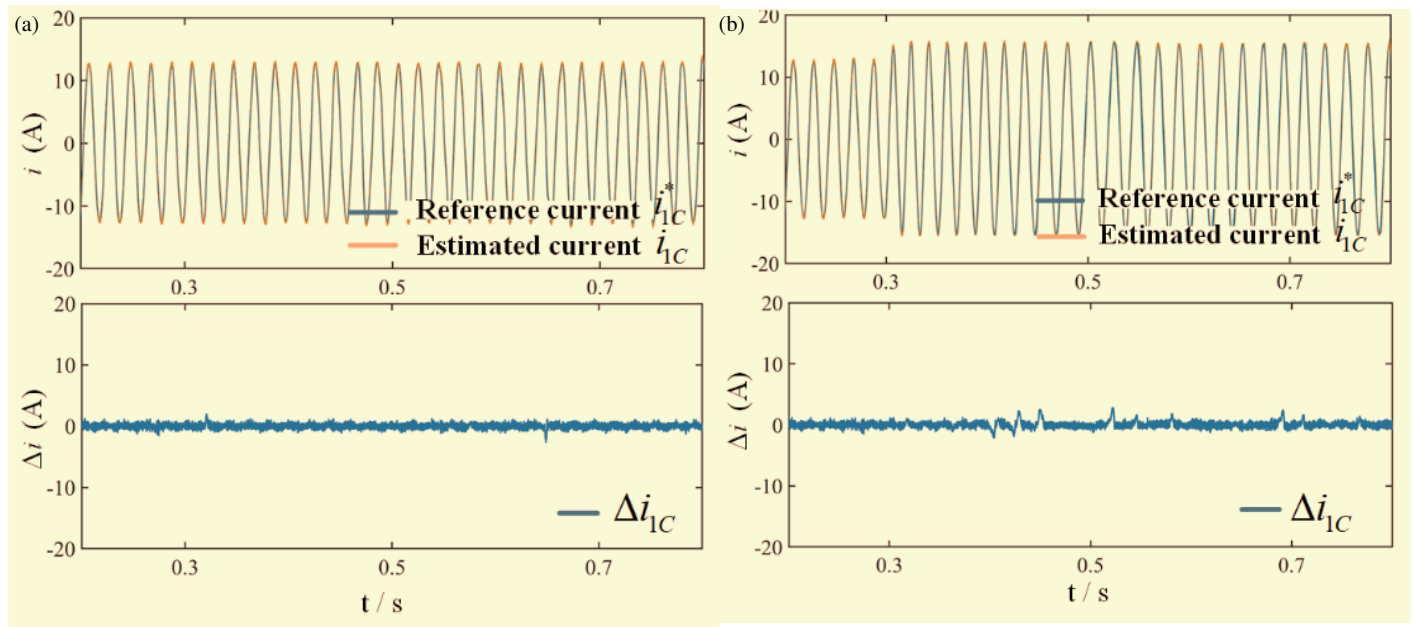

FIGURE 12. Simulation diagram of BIM running with constant speed and sudden load. (a) Rated speed, no load. (b) Rated speed, sudden load.

erence current in Fig. 11(b). The current frequency is closest to the rated current frequency when the speed is closest to the rated speed. At different speed stages, the estimated current fluctuation ranges were $(-0.99\,\text{A}, 0.5\,\text{A})$, $(-0.85\,\text{A}, 0.81\,\text{A})$, $(-1.1\,\text{A}, 1.2\,\text{A})$, and $(-0.95\,\text{A}, 0.99\,\text{A})$, respectively. When the speed changes, the current reconstructed by the VCS can maintain the following characteristics.

5.2.3. Analysis of Sudden Load Operation

To research the estimated current under the FTC when the load changed, the load was added suddenly after the BIM runs for $0.3\,\text{s}$ without load. Fig. 12(a) and Fig. 12(b) illustrate the simulation diagrams of the estimated current, reference current, and their errors under the conditions of the rated speed and sudden load. It can be seen that after the load was applied, the given current and estimated current both rose, and the average error
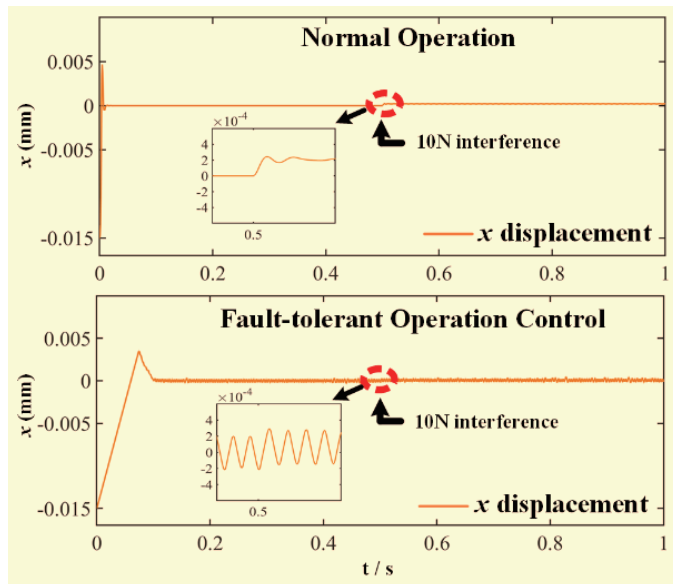
FIGURE 13. x-direction displacement of rotor before and after FTC operation.

FIGURE 14. y-direction displacement of rotor before and after FTC operation.

range of the current created when the load was applied abruptly was $(-0.93\,A, 1.75\,A)$. Under conditions of constant speed and sudden load, it can be shown that the fault current can be substituted with the estimated current.

5.3. Analysis of Rotor Suspension Performance

To study the suspension performance of the rotor under fault-tolerant operational control, the rotor displacement before and after the FTC was simulated. When the BIM runs to 0.5 s, a 10 N interference force is applied to the x-axis direction of the rotor. The displacement in the x-axis direction under normal operation and fault-tolerant operation is shown in Fig. 13. After the interference force was applied during normal operation, it can be seen that the displacement in the x direction was between 1.65×10^{-4} mm and 2.45×10^{-4} mm. In the fault-tolerant operation control, the fluctuation range was -1.6×10^{-4} mm to 2.95×10^{-4} mm. After the interference force was applied, the x-direction displacement error was 0.5×10^{-4} mm $\sim 3.25 \times 10^{-4}$ mm, which was much less than the rotor air gap. The displacement along the y-axis of the rotor is shown in Fig. 14. During normal operation, the y-direction displacement fluctuates in the range of -1×10^{-4} mm to -1.7×10^{-4} mm, and the displacement range after FTC was -2.2×10^{-4} mm to $+2.7 \times 10^{-4}$ mm. The y-direction displacement error was 1×10^{-4} mm to 1.2×10^{-4} mm, which was also much less than the rotor air gap. It is shown that under fault-tolerant operation control, the good suspension performance of the rotor in x and y directions can still be maintained after the interference is applied to the rotor.
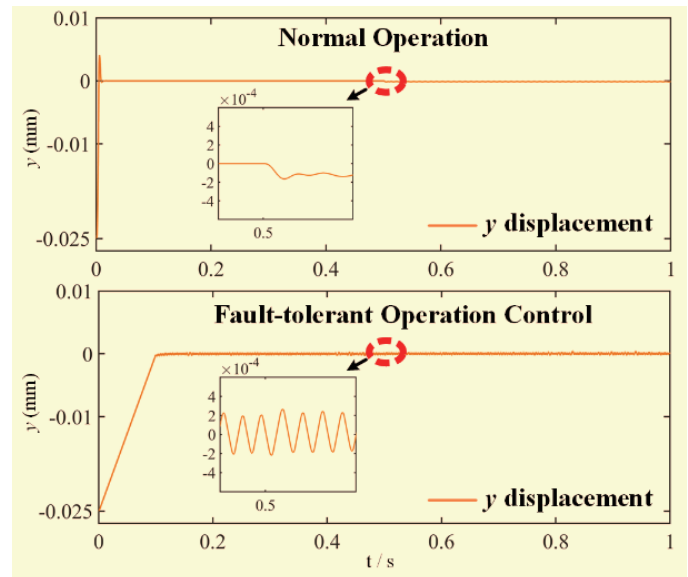
6. EXPERIMENT VERIFICATION

To further verify the effectiveness of the proposed VCS in the fault-tolerant operation control of BIM, the experimental platform built by the research group as shown in Fig. 15 was used for experimental research. A block diagram of the FTC experiment is shown in Fig. 16.

First, the estimated current of the VCS system is analyzed experimentally. In Fig. 17, the A-phase current of the BIM torque winding is depicted during the no-load operation; it is a standard sinusoidal waveform with a steady amplitude of 13.36 A. As shown in Fig. 18, the VCS current has a few burrs and variations when the control system enters fault-tolerant operation control owing to the current sensor failure, and the final amplitude is stable at 14.01 A with an error rate of 4.87%. As shown in Fig. 19, when the state observer is used for fault tolerance control, its estimated current amplitude is 14.69 A, and the error rate is 9.96%. In contrast, VCS's fault-tolerant control strategy is better for current estimation, and the effectiveness of the estimated current of the VCS system was verified.

Then the current performance of the BIM under a sudden load before and after fault tolerance was verified. As shown in Fig. 20, the stator A-phase current amplitude maintains stability before fault tolerance and increases and maintains a new steady state after the load is applied, which is consistent with the simulation results. The fault-tolerant current of a sudden 10 N·m loading in the FTC is shown in Fig. 21. Before sudden loading, the fault-tolerant current was consistent with the current in Fig. 20, and the current amplitude increased after sudden loading. The simulated results and experimental results corresponded with each other. The effectiveness of the fault-tolerant current under a sudden load is verified.

Second, the speed performance of BIM under FTC was experimentally verified. As shown in Fig. 22, the speed waveform
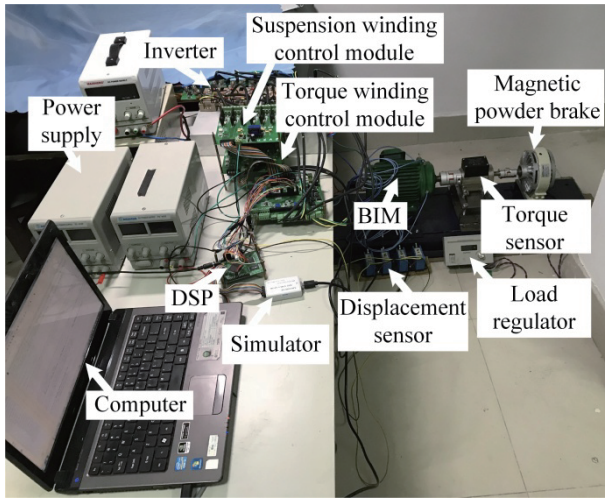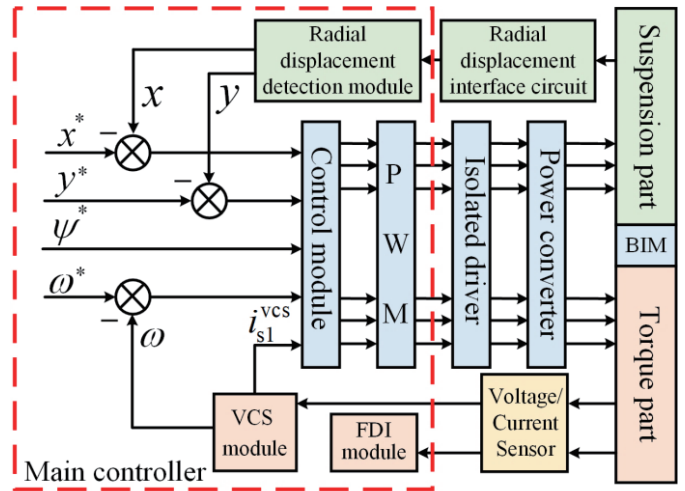
FIGURE 15. The experiment platform.

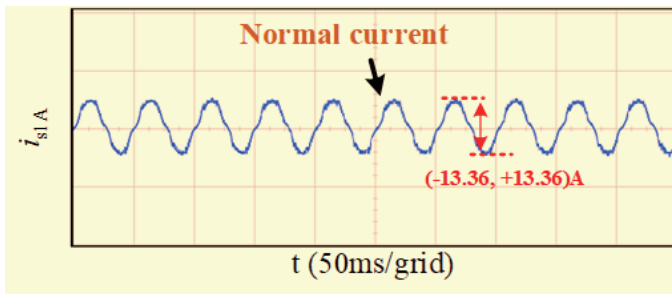FIGURE 16. Experimental control block diagram.

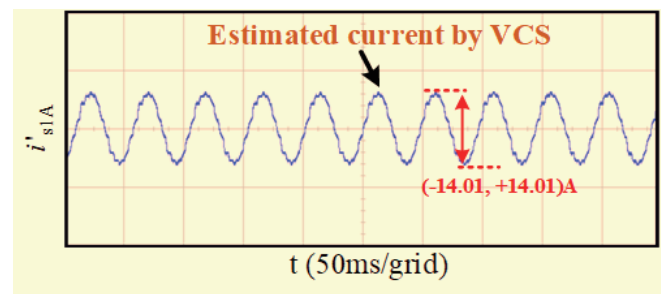FIGURE 17. Phase A current under no load.

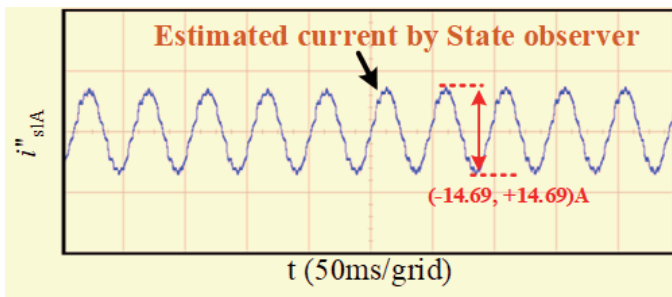FIGURE 18. VCS current under no load.

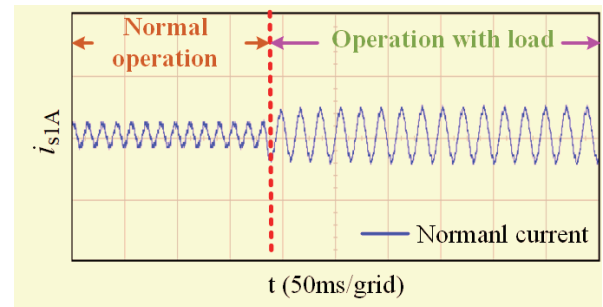FIGURE 19. State observer current under no load.

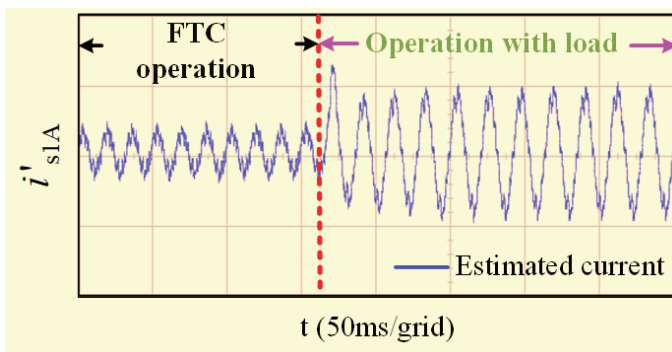FIGURE 20. Phase current of sudden load under normal operation.
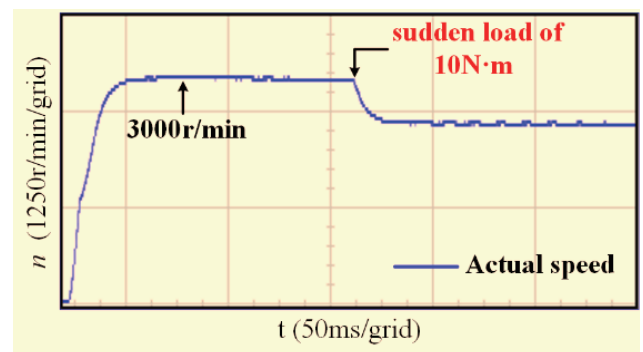

FIGURE 21. Phase current of sudden load under FTC.

FIGURE 22. Speed of sudden load.
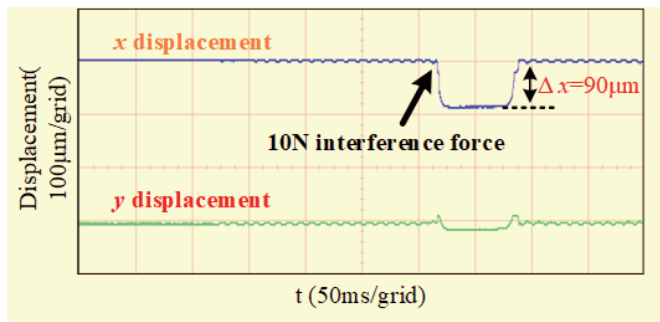
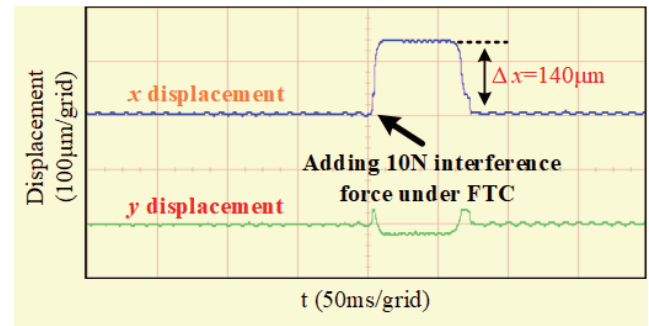**FIGURE 23**. Displacement in x and y directions under normal operation.

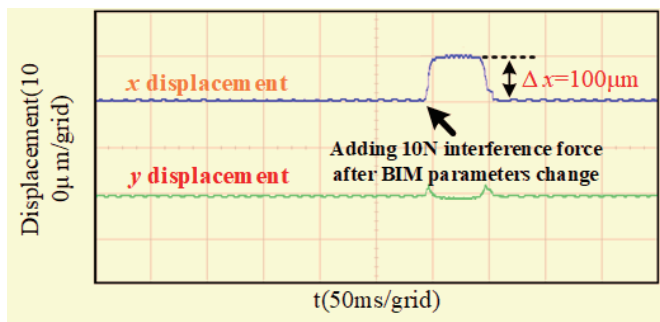**FIGURE 24**. Displacement in x and y directions under FTC.

FIGURE 25. Displacement in x and y directions under parameters change.
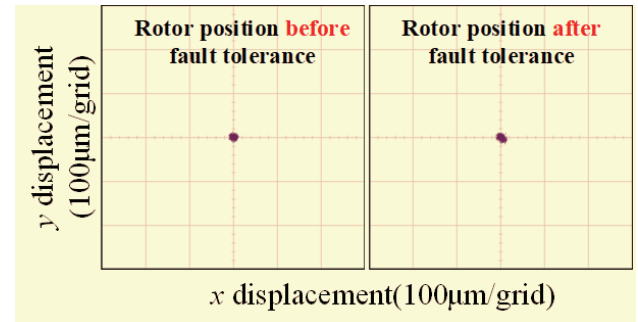

FIGURE 26. Rotor position before and after fault tolerance.

fluctuated to some extent under fault-tolerant operation, but it was basically consistent with the given speed waveform. After stable operation at 3000 r/min, a 10 N·m load was suddenly added, and the motor speed decreased, but it could still be stably maintained at 2450 r/min in the end. In the case of a sudden load in a fault-tolerant operation, the speed performance of the BIM can be well maintained after the VCS system is adopted.

Finally, the effect of BIM on suspension performance during FTC operation was tested experimentally. As shown in Fig. 23, the displacement changed significantly under normal operation after the BIM rotor was disturbed; however, it was still less than the motor air gap. Fig. 24 depicts a slight vibration of the BIM rotor displacement waveform in the x and y directions during fault-tolerant operation, and the experimental results are consistent with the simulated ones After a 10 N interference force was applied in the x direction, the rotor was displaced in a short time certain vibrations occurred in both x and y directions; the vibration amplitude was slightly larger than the displacement under normal operation, but it was less than the motor air gap value of 375 μm. Finally, a stable suspension state before interference was maintained by the rotor.

As can be seen from Fig. 25, when BIM parameters change, the deviation after disturbance in the x direction is 100 μm, which is far less than the motor air gap, and the stable suspension state is restored within 50 ms. Therefore, when BIM parameters change, the FTC strategy proposed in this paper can still meet the anti-disturbance performance of BIM.

The motion range of the rotor after the fault tolerance was slightly expanded compared with that before fault tolerance, as shown in Fig. 26, but the motion range was much smaller than the motor air gap. It can be observed that BIM can still be maintained in a stable suspension under fault tolerant operation control.

7. CONCLUSION

This study proposes a fault detection method and an FTC strategy based on VCS for BIM, and the following conclusions have been obtained:

1) The current sensor failure in the BIM control system can be located quickly and precisely using the coordinate transformation-based fault detection method. It is simple in design, fast in calculation, and can intuitively identify the fault locations, which is feasible in the field of BIM sensor fault detection

2) The VCS can effectively reconstruct the faulty current, and the reconstructed current can minimize the winding coupling impact and guarantee that the BIM has a specific suspension performance after sensor failure. The proposed strategy has a simple design and does not require the processing of a large amount of data, which can guarantee a specific suspension performance. This is an effective FTC strategy for BIM.

3) Results from simulations and experiments indicated that fault markers can detect current sensor faults quickly and precisely and were suitable for dealing with faulty problems. Moreover, the feedback current can be better reconfigured by the VCS, and suspension performance was ensured after the current sensor fault, as well as its practicability.

ACKNOWLEDGEMENT

REFERENCES

[1] Jin, Z., X. Sun, L. Chen, and Z. Yang, "Robust multi-objective optimization of a 3-pole active magnetic bearing based on combined curves with climbing algorithm," *IEEE Transactions on Industrial Electronics*, Vol. 69, No. 6, 5491–5501, Jun. 2022.

[2] Yang, Z., C. Sun, X. Sun, and Y. Sun, "An improved dynamic model for bearingless induction motor considering rotor eccentricity and load change," *IEEE Transactions on Industrial Electronics*, Vol. 69, No. 4, 3439–3448, Apr. 2022.

[3] Sun, X., Z. Jin, Y. Cai, Z. Yang, and L. Chen, "Grey wolf optimization algorithm based state feedback control for a bearingless permanent magnet synchronous machine," *IEEE Transactions on Power Electronics*, Vol. 35, No. 12, 13 631–13 640, Dec. 2020.

[4] Wang, W., W. Tian, Z. Wang, W. Hua, and M. Cheng, "A fault diagnosis method for current sensors of primary permanent-magnet linear motor drives," *IEEE Transactions on Power Electronics*, Vol. 36, No. 2, 2334–2345, Feb. 2021.

[5] Farhadi, M., M. T. Fard, M. Abapour, and M. T. Hagh, "DC–AC converter-fed induction motor drive with fault-tolerant capability under open-and short-circuit switch failures," *IEEE Transactions on Power Electronics*, Vol. 33, No. 2, 1609–1621, Feb. 2018.

[6] Shi, Z., X. Sun, Y. Cai, and Z. Yang, "Robust design optimization of a five-phase PM hub motor for fault-tolerant operation based on Taguchi method," *IEEE Transactions on Energy Conversion*, Vol. 35, No. 4, 2036–2044, Dec. 2020.

[7] Zhou, D., Y. Li, J. Zhao, F. Wu, and H. Luo, "An embedded closed-loop fault-tolerant control scheme for nonredundant VSI-fed induction motor drives," *IEEE Transactions on Power Electronics*, Vol. 32, No. 5, 3731–3740, May 2017.

[8] Li, Z., P. Wheeler, A. Watson, A. Costabeber, B. Wang, Y. Ren, Z. Bai, and H. Ma, "A fast diagnosis method for both IGBT faults and current sensor faults in grid-tied three-phase inverters with two current sensors," *IEEE Transactions on Power Electronics*, Vol. 35, No. 5, 5267–5278, May 2020.

[9] Kommuri, S. K., M. Defoort, H. R. Karimi, and K. C. Veluvolu, "A robust observer-based sensor fault-tolerant control for PMSM in electric vehicles," *IEEE Transactions on Industrial Electronics*, Vol. 63, No. 12, 7671–7681, Dec. 2016.

[10] Sun, X., Y. Xiong, M. Yao, and J. Wu, "High fault-tolerance evaluation on position signal for switched reluctance motor drives," *IEEE Transactions on Energy Conversion*, Vol. 37, No. 3, 1844–1853, Sep. 2022.

[11] Bourogaoui, M., H. B. A. Sethom, and I. S. Belkhodja, "Speed/position sensor fault tolerant control in adjustable speed drives — A review," *ISA Transactions*, Vol. 64, 269–284, Sep. 2016.

[12] Sun, X., T. Li, X. Tian, and J. Zhu, "Fault-tolerant operation of a six-phase permanent magnet synchronous hub motor based on model predictive current control with virtual voltage vectors," *IEEE Transactions on Energy Conversion*, Vol. 37, No. 1, 337–346, Mar. 2022.

[13] Climente-Alarcon, V., J. A. Antonino-Daviu, M. Riera-Guasp, and M. Vlcek, "Induction motor diagnosis by advanced notch FIR filters and the Wigner — Ville distribution," *IEEE Transactions on Industrial Electronics*, Vol. 61, No. 8, 4217–4227, Aug. 2014.

[14] Petersen, N., A. Khamitov, T. Slininger, and E. L. Severson, "Machine design and precision current regulation for the parallel DPNV bearingless motor winding," *IEEE Transactions on Industry Applications*, Vol. 57, No. 6, 7000–7011, Nov. 2021.

[15] Tsukada, N., T. Onaka, J. Asama, A. Chiba, and T. Fukao, "Novel coil arrangement of an integrated displacement sensor with reduced influence of suspension fluxes for a wide gap bearingless motor," *IEEE Transactions on Industry Applications*, Vol. 46, No. 6, 2304–2310, 2010.

[16] Ooshima, M., A. Chiba, A. Rahman, and T. Fukao, "An improved control method of buried-type IPM bearingless motors considering magnetic saturation and magnetic pull variation," *IEEE Transactions on Energy Conversion*, Vol. 19, No. 3, 569–575, Sep. 2004.

[17] Sun, X., F. Cai, Z. Yang, and X. Tian, "Finite position control of interior permanent magnet synchronous motors at low speed," *IEEE Transactions on Power Electronics*, Vol. 37, No. 7, 7729–7738, Jul. 2022.

[18] Xu, S., W. Huang, H. Wang, W. Zheng, J. Wang, Y. Chai, and M. Ma, "A simultaneous diagnosis method for power switch and current sensor faults in grid-connected three-level NPC inverters," *IEEE Transactions on Power Electronics*, Vol. 38, No. 1, 1104–1118, Jan. 2023.

[19] Yang, Z., T. Xu, X. Sun, J. Jia, and H. Zhu, "Sensor fault diagnosis and fault-tolerant control of a bearing less induction motor Based on BPNN," *Proceedings of the CSEE*, Vol. 42, No. 11, 4218–4227, 2022.

[20] Xu, S., X. Chen, F. Liu, H. Wang, Y. Chai, W. X. Zheng, and H. Chen, "A novel adaptive SMO-based simultaneous diagnosis method for IGBT open-circuit faults and current sensor incipient faults of inverters in PMSM drives for electric vehicles," *IEEE Transactions on Instrumentation and Measurement*, Vol. 72, 3526915, Aug. 2023.

[21] Azzoug, Y., M. Sahraoui, R. Pusca, T. Ameid, R. Romary, and A. J. M. Cardoso, "High-performance vector control without AC phase current sensors for induction motor drives: Simulation and real-time implementation," *ISA Transactions*, Vol. 109, 295–306, Mar. 2021.

[22] Huo, M., H. Luo, C. Cheng, K. Li, S. Yin, O. Kaynak, J. Zhang, and D. Tang, "Subspace-aided sensor fault diagnosis and compensation for industrial systems," *IEEE Transactions on Industrial Electronics*, Vol. 70, No. 9, 9474–9482, Sep. 2023.

[23] Mehmood, F., P. M. Papadopoulos, L. Hadjidemetriou, A. Charalambous, and M. M. Polycarpou, "Model-based fault diagnosis scheme for current and voltage sensors in grid side converters," *IEEE Transactions on Power Electronics*, Vol. 38, No. 4, 5360–5375, Apr. 2023.

[24] Chen, J., Y. Fujii, M. W. Johnson, A. Farhan, and E. L. Severson, "Optimal design of the bearingless induction motor," *IEEE Transactions on Industry Applications*, Vol. 57, No. 2, 1375–1388, 2021.

[25] Jin, Z., X. Sun, L. Chen, and Z. Yang, "Robust multi-objective optimization of a 3-pole active magnetic bearing based on combined curves with climbing algorithm," *IEEE Transactions on Industrial Electronics*, Vol. 69, No. 6, 5491–5501, Jun. 2022.

[26] Ding, Q., Z. Yang, X. Sun, and C. Lu, "Correction of the suspension force expression and the control compensation study in a bearingless induction motor," *Electrical Engineering*, Vol. 104,

No. 4, 2457–2469, 2022.

[27] Jankowska, K. and M. Dybkowski, "A current sensor fault tolerant control strategy for PMSM drive systems based on Cri markers," *Energies*, Vol. 14, No. 12, 3443, Jun. 2021.

[28] Adamczyk, M. and T. Orlowska-Kowalska, "Virtual current sensor in the fault-tolerant field-oriented control structure of an induction motor drive," *Sensors*, Vol. 19, No. 22, 4979, Nov. 2019.

[29] Adamczyk, M. and T. Orlowska-Kowalska, "Postfault direct field-oriented control of induction motor drive using adaptive virtual current sensor," *IEEE Transactions on Industrial Electronics*, Vol. 69, No. 4, 3418–3427, Apr. 2022.